



Staggered-grid split-node method for spontaneous rupture simulation

Luis A. Dalguer,¹ and Steven M. Day¹

Received 24 April 2006; revised 27 September 2006; accepted 10 October 2006; published 15 February 2007.

[1] We adapt the traction-at-split-node method for spontaneous rupture simulations to the velocity-stress staggered-grid finite difference scheme. The staggered-grid implementation introduces both velocity and stress discontinuities via split nodes. The staggered traction components on the fault plane are interpolated to form the traction vector at split nodes, facilitating alignment of the vectors of sliding friction and slip velocity. To simplify the split-node partitioning of the equations of motion, spatial differencing is reduced from fourth to second order along the fault plane, but in the remainder of the grid the spatial differencing scheme remains identical to conventional spatially fourth-order three-dimensional staggered-grid schemes. The resulting staggered-grid split node (SGSN) method has convergence rates relative to rupture-time, final-slip, and peak-slip-velocity metrics that are very similar to the corresponding rates for both a partly staggered split-node code (DFM) and the boundary integral method. The SGSN method gives very accurate solutions (in the sense that errors are comparable to the uncertainties in the reference solution) when the median resolution of the cohesive zone is 4.4 grid points. Combined with previous results for other grid types and other fault-discontinuity approximations, the SGSN results demonstrate that accuracy in finite difference solutions to the spontaneous rupture problem is controlled principally by the scheme used to represent the fault discontinuity, and is relatively insensitive to the grid geometry used to represent the continuum. The method provides an efficient and accurate means of adding spontaneous rupture capability to velocity-stress staggered-grid finite difference codes, while retaining the computational advantages of those codes for problems of wave propagation in complex media.

Citation: Dalguer, L. A., and S. M. Day (2007), Staggered-grid split-node method for spontaneous rupture simulation, *J. Geophys. Res.*, 112, B02302, doi:10.1029/2006JB004467.

1. Introduction

[2] Accurate numerical simulation of the dynamic rupture process in realistic three-dimensional models is important to our understanding of the physics of earthquakes, and is likely to assume increasing importance in the modeling of strong ground motion. Suitable numerical solution techniques for the spontaneous rupture problem can be built into elastodynamic methods based upon, for example, finite difference (FD), finite element (FE), spectral element (SE), or boundary integral (BI) methods. Each of these numerical methods can be implemented on any of several different grid types, and the elastodynamic equations solved to any specified order of accuracy. However, recent work by Day *et al.* [2005] (hereafter D05) and Dalguer and Day [2006] has shown, at least in the case of the most widely used FD-based methods, that solution accuracy is controlled principally by the numerical formulation of the jump conditions on the fault discontinuity. In that study, neither grid type nor order of spatial differencing in the grid is found to

have a significant effect on spontaneous-rupture solution accuracy, but the method of approximation of the jump conditions has a very large effect. It is likely that a similar conclusion will hold for other solution methods such as FE and SE.

[3] Methods which represent the fault discontinuity by explicitly incorporating discontinuity terms at velocity nodes in the grid are called traction-at-split-node (TSN) methods [Andrews, 1973, 1999; Day, 1977, 1982b]. Interactions between the halves of the “split nodes” occur exclusively through the tractions (frictional resistance and normal traction) acting between them, and these in turn are controlled by the jump conditions and a friction law. The TSN is usually implemented in schemes that (1) employ second-order spatial differencing, and (2) locate all three velocity components at a common set of grid vertices, with all six stress components collocated at the corresponding cell centroids. This description applies to the so-called “partly staggered” FD schemes, in the terminology of Moczo *et al.* [2006], as well as to some FE schemes. The prevalence of the TSN fault representation in methods meeting these criteria is probably due to the ease with which these methods permit a partition of the equations of motion into separate parts governing each side of the fault surface [Day *et al.*, 2005, Appendix A].

¹Department of Geological Sciences, San Diego State University, San Diego, California, USA.

[4] The TSN method has not previously been applied to model spontaneous rupture in staggered-grid 3D FD methods such as the fourth-order velocity-stress staggered (VSSG) scheme that is widely used for elastodynamics problems [e.g., *Madariaga*, 1976; *Levander*, 1988; *Graves*, 1996]. The VSSG scheme defines each component of shear stress and particle velocity at a different grid point, and the normal stresses share another grid position. This geometrical complexity, plus the fact that the VSSG scheme is often implemented with fourth-order differencing, inhibits, or at least obscures, the partitioning required by the TSN method (but note that *Madariaga's* [1976] VSSG method for fixed-rupture-velocity modeling is effectively a split-node scheme specialized to a problem with symmetry across the fault plane). Instead, the VSSG schemes have been adapted to solve spontaneous rupture problems through what *Dalguer and Day* [2006] called “inelastic-zone” models [e.g., *Madariaga et al.*, 1998; *Andrews*, 1976a, 1999]. That is, the fault discontinuity is represented through inelastic increments to stress components at a set of stress grid points taken to lie on the fault plane. With this type of scheme, the fault surface is indistinguishable from an inelastic zone with a thickness given by the spatial step Δx (or an integral multiple of Δx). The well-known examples of inelastic-zone schemes are the “thick fault” (TF) method proposed by *Madariaga et al.* [1998], and the “stress glut” (SG) method first presented by *Andrews* [1976a] for modeling yielding off the fault, and subsequently described by *Andrews* [1999]. The inelastic-zone methods are very easy to implement in existing VSSG wave propagation codes, as no modification to the difference equations is required, only modifications to the way stress is calculated from strain rate. However, we have found [*Dalguer and Day*, 2004, 2006] that the inelastic-zone TF and SG methods show much poorer performance than does the TSN formulation. In a 3D test, the SG inelastic-zone method achieved solutions that are qualitatively meaningful and quantitatively reliable to within a few percent, but full convergence is uncertain, and SG proved to be highly inefficient computationally, relative to the TSN approach. The TF inelastic-zone method did not achieve qualitatively meaningful solutions to the 3D test problem, in the sense that, for example, TF solutions exhibited rupture-velocity fluctuations not present in the reference solution, had a much lower average rupture velocity, and did not match the shape of the rupture-front stress concentration. The method proved to be sufficiently computationally inefficient that it was not feasible to explore convergence quantitatively.

[5] In the present paper, we propose a version of the TSN formulation for the VSSG FD scheme. Our starting point is the standard VSSG elastodynamic FD scheme with fourth-order spatial differencing. We follow an approach similar to that described in D05 to partition the difference equations into separate sets for the two sides of the fault. However, because of the characteristics of the VSSG scheme, some additional steps are necessary: (1) The spatial differencing along the fault plane is reduced to second order. (2) In addition to splitting the fault-plane velocity nodes into plus- and minus-side parts, those stress points that lie on the fault plane, and at which are located stress components that are not continuous across the fault (i.e., those that are not fault-plane traction components) are also split into plus-side and

minus-side parts. We used the 3D, fourth-order VSSG wave propagation code of *Pitarka* [1999] as our starting point. The resulting method will be referred to as the SGSN (staggered-grid split-node) method.

[6] The accuracy of the SGSN method is verified following the methodology of D05. These authors performed a detailed comparison of solutions to the *Harris et al.* [2004] benchmark problem as calculated, respectively, by two independent numerical methods, a boundary integral (BI) method and a TSN method called DFM [*Day*, 1982a, 1982b; *Day and Ely*, 2002]. They found that the BI and DFM methods converge, with decreasing spatial discretization interval Δx , to a common solution, to within well-defined tolerances, for three specific error metrics: the RMS differences of rupture time, slip rate and final slip.

[7] We perform the assessment of the SGSN method by using it to compute solutions to the *Harris et al.* [2004] benchmark problem. Then, using the D05 numerical solution as a reference, we compute the three error metrics proposed in that study, and examine their dependence upon Δx . We find that the SGSN method is convergent, with the same convergence rate (for the rupture-time metric) as the BI and DFM methods. It is highly efficient, requiring only about two-grid-point resolution of the rupture-front cohesive zone to reach RMS rupture-time error smaller than 0.7%.

2. Fault Jump Conditions

[8] The idealization of the earthquake source rupture as a dynamically running shear crack on a frictional interface embedded in a linearly elastic continuum is widely accepted as a useful idealization in earthquake physics research [e.g., *Kostrov*, 1964, 1966; *Andrews*, 1976a, 1976b; *Das and Aki*, 1977; *Day*, 1982a, 1982b; *Fukuyama and Madariaga*, 1998; *Harris and Day*, 1999; *Dalguer et al.*, 2001]. The theoretical study of this problem class is usually possible only with computationally intensive numerical methods that solve the elastodynamic equations of motion in the continuum, coupling them to additional equations governing frictional sliding on the boundary representing the fault surface. This leads to a boundary value problem in which the shear traction that acts at the frictional interface during rupture is conditioned to follow a constitutive law.

[9] We orient the fault by a choice of fault-normal direction, and define negative and positive sides of the fault such that the normal vector is directed from the former toward the latter. Denoting the shear traction vector on the fault (traction exerted by the positive side upon the negative side) by τ , the tangential displacement discontinuity (slip) vector (displacement of positive side relative to negative side) by \mathbf{s} , their respective magnitudes by τ and s , and the frictional shear strength by τ_c , the fault jump conditions can be formulated in the form given by D05 as:

$$\tau_c - \tau \geq 0 \quad (1)$$

$$\tau_c \dot{\mathbf{s}} - \tau \dot{\mathbf{s}} = 0. \quad (2)$$

Equation (1) stipulates that the shear traction be bounded by the (current value of) frictional strength, and equation (2) stipulates that any nonzero velocity discontinuity be opposed by an antiparallel traction (i.e., the negative side

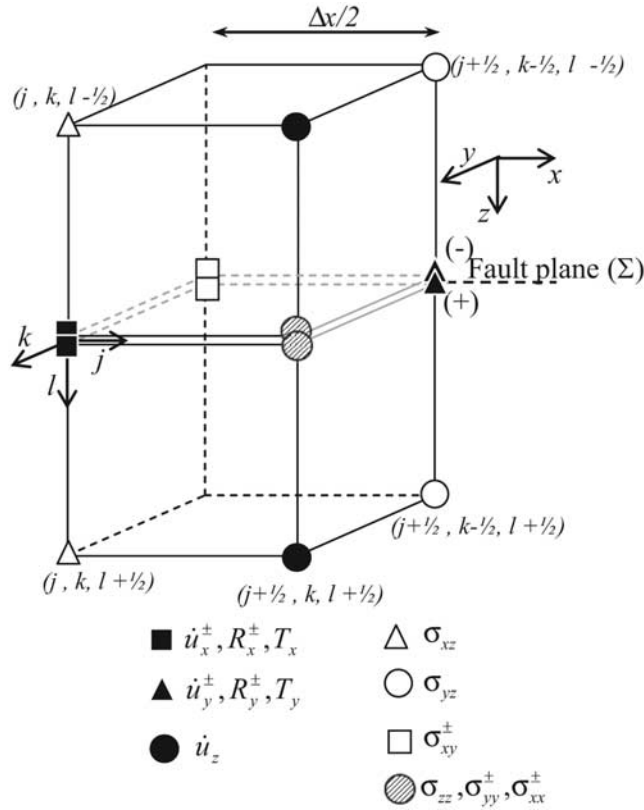


Figure 1. Staggered-grid split-node geometry, illustrated for grid cells adjacent to the fault in the VSSG scheme. The fault plane grid points for \dot{u}_x , \dot{u}_y , σ_{xx} , σ_{yy} , and σ_{xy} are split into plus-side and minus-side parts. The finite difference equations of motion are partitioned to form separate elastic restoring forces (R) acting on the two halves. The two halves of a split velocity node interact only through shear tractions (T) at that node point.

exerts traction $-\tau$ on the positive side) with magnitude equal to the frictional strength τ_c .

[10] The frictional shear strength τ_c evolves according to some specified friction law, and may depend upon normal stress, slip, slip velocity, and other mechanical or thermal variables. Here we use the simple slip-weakening friction model in the form given by *Andrews* [1976a, 1976b]. This friction law, first proposed by *Ida* [1972], is extensively used for shear dynamic rupture simulations [e.g., *Andrews*, 1976a, 1976b; *Day*, 1982b; *Olsen et al.*, 1997; *Fukuyama and Madariaga*, 1998; *Madariaga et al.*, 1998; *Harris and Day*, 1999; *Dalguer et al.*, 2003a, 2003b].

[11] The frictional strength τ_c is assumed to be proportional to normal stress σ_n (taken negative in compression)

$$\tau_c = -\mu_f(\ell)\sigma_n. \quad (3)$$

The coefficient of friction $\mu_f(\ell)$ depends on the slip path length, $\ell = \int_0^t \dot{s}(t') dt'$, through the linear slip-weakening relationship

$$\mu_f(\ell) = \begin{cases} \mu_s - (\mu_s - \mu_d)\ell/d_0 & \ell < d_0 \\ \mu_d & \ell \geq d_0 \end{cases}, \quad (4)$$

where μ_s and μ_d are coefficients of static and dynamic friction, respectively, and d_0 is the critical slip-weakening distance. Despite its limitations as a model for natural earthquakes (as noted in, e.g., D05), this friction law provides a suitable starting point for testing numerical methods.

[12] The jump conditions (1)–(2) combined with the friction law (3)–(4), define our idealized model for fault behavior.

3. Staggered-Grid Split-Node (SGSN) Method

[13] The FD scheme solves the velocity-stress form of the equations of elastodynamics, in which Cartesian components of the velocity vector $\dot{\mathbf{u}}$ and stress tensor σ are the dependent variables:

$$\partial_t \dot{\mathbf{u}} = \rho^{-1} \nabla \sigma \quad (5a)$$

$$\partial_t \sigma = \lambda(\nabla \cdot \dot{\mathbf{u}}) \mathbf{I} + \mu(\nabla \dot{\mathbf{u}} + \dot{\mathbf{u}} \nabla), \quad (5b)$$

where λ and μ are the Lamé constants, ρ is density, and \mathbf{I} is the identity tensor. Figure 1 shows the staggered-grid FD geometry. The fault is an x, y plane and the fault normal is in the z direction. Indices for \dot{u}_x grid points are integer triples (j, k, l) , and indices for other velocity and stress components are offset from this by half-integer values in one or more directions, as shown in Figure 1. Material constants (densities and Lamé constants λ and μ) are assigned at points with indices $(j, k + 1/2, l + 1/2)$. In the figure, the grid points above and below the fault (which is the central horizontal plane in the figure) constitute a quarter of a unit cell; that is, the region depicted has extent Δx in the fault-normal direction and $\Delta x/2$ in the fault-parallel directions. In our notation, grid indices are denoted by Roman subscripts, with (j, k, l) always representing integers (other Roman subscripts may take on half-integer or integer values), and Greek subscripts denote Cartesian components (x, y , or z). Where there is no ambiguity, we will sometimes suppress the grid indices.

[14] Note (Figure 1) that, of the nine independent velocity and stress components, six have grid locations on fault plane: the tangential velocities (\dot{u}_x and \dot{u}_y) and the stress components σ_{xy} , σ_{xx} , σ_{yy} , and σ_{zz} . Of these, five (all except σ_{zz}) become discontinuous across the fault plane when slip is permitted. To accommodate the field discontinuities, these five variables, when they occur on the fault plane, are therefore split into plus-side and minus-side parts (denoted by \dot{u}_x^\pm , \dot{u}_y^\pm , σ_{xy}^\pm , σ_{xx}^\pm , and σ_{yy}^\pm) in our scheme. We let l_0 denote the l index of the fault plane, and suppress this index when referring to split variables.

[15] In forming FD approximations to (5a) and (5b), the time derivatives are approximated by second-order central differences,

$$\partial_t \dot{\mathbf{u}}(t) \approx 1/\Delta t [\dot{\mathbf{u}}(t + \Delta t/2) - \dot{\mathbf{u}}(t - \Delta t/2)] \quad (6a)$$

$$\partial_t \sigma(t - \Delta t/2) \approx 1/\Delta t [\sigma(t) - \sigma(t - \Delta t)], \quad (6b)$$

as in most previous work [e.g., *Graves*, 1996]. The density and reciprocals of the Lamé constants are evaluated at the required grid points by linear interpolation, as in the work by *Graves* [1996]. *Moczo et al.* [2002] have shown that

improved accuracy is achieved in heterogeneous media by employing local model averages at each velocity point (for density) and stress point (for reciprocal Lamé constants), and it would be straightforward to incorporate this refinement into our scheme as well. The present scheme reduces to that of Moczo et al. when the model consists of homogeneous blocks with interfaces at grid planes not containing those grid points at which we define material constants (one important special case in which the schemes are equivalent is when a material-properties interface coincides with the fault plane).

3.1. Interior Grid Points

[16] To approximate the spatial derivatives at interior points (i.e., points not on the fault plane), we distinguish the following four cases, in order to avoid using discontinuous quantities in the difference approximations to the spatial derivatives.

[17] 1. At any point located at a distance of at least $2\Delta x$ from the fault plane, we approximate each spatial derivative in (5a) and (5b) with a fourth-order spatial difference operator, denoted $D_\nu^{(4)}$, $\nu = x, y, z$. In the following, we let ϕ represent an arbitrary stress or velocity component. For z derivatives we use the approximation

$$\begin{aligned} (\partial_z \phi)_{j,k,l} &\approx \Delta x^{-1} \left(D_z^{(4)} \phi \right)_{j,k,l} \\ &= \Delta x^{-1} \left[\frac{9}{8} \left(\phi_{j,k,l+1/2} - \phi_{j,k,l-1/2} \right) \right. \\ &\quad \left. - \frac{1}{24} \left(\phi_{j,k,l+3/2} - \phi_{j,k,l-3/2} \right) \right], \quad |l - l_0| \geq 2, \end{aligned} \quad (7a)$$

for the case of derivatives centered at integer values of the indices, and similar expressions for x and y derivatives. With substitution of appropriate half-integer indices, 7a is also used for derivatives centered at half-integer, instead of integer, values of the indices (i.e., with $j + 1/2$ in place of j , etc). At the stipulated distance from the fault, this difference operator acts on points confined to only one side of the fault plane (i.e., confined to only one of the two volumes separated by the fault plane). Therefore the split nodes are not involved in the calculation of the derivative, and our method reduces to a conventional staggered fourth-order 3D elastodynamic scheme [e.g., *Graves, 1996*].

[18] 2. At any point located at a distance of exactly $3\Delta x/2$ from the fault plane, we approximate each spatial derivative in (5a) and (5b) with the same fourth-order spatial difference operator as before, but now the difference approximation to the derivative with respect to the z coordinate involves a value of the field variable on the fault plane. For that fault plane value, we use the corresponding half of the fault plane split node for that variable. That is, z difference operators centered on the plus sides of the fault use the plus-side split-node variable values, for example,

$$\begin{aligned} (\partial_z \phi)_{j,k,l_0+3/2} &\approx \Delta x^{-1} \left(D_z^{(4)} \phi \right)_{j,k,l} \\ &= \Delta x^{-1} \left[\frac{9}{8} \left(\phi_{j,k,l_0+2} - \phi_{j,k,l_0+1} \right) \right. \\ &\quad \left. - \frac{1}{24} \left(\phi_{j,k,l_0+3} - \phi_{j,k,l_0}^+ \right) \right]. \end{aligned} \quad (7b)$$

Similarly, those centered on the minus side use minus-side split-node values

$$\begin{aligned} (\partial_z \phi)_{j,k,l_0-3/2} &\approx \Delta x^{-1} \left(D_z^{(4)} \phi \right)_{j,k,l} \\ &= \Delta x^{-1} \left[\frac{9}{8} \left(\phi_{j,k,l_0-1} - \phi_{j,k,l_0-2} \right) \right. \\ &\quad \left. - \frac{1}{24} \left(\phi_{j,k,l_0-3}^- - \phi_{j,k,l_0-3} \right) \right]. \end{aligned} \quad (7b')$$

[19] 3. At any point located at distance Δx from the fault plane, we approximate each spatial derivative with a second-order spatial difference, denoted $D_\nu^{(2)}$, $\nu = x, y, z$, for example,

$$\begin{aligned} (\partial_z \phi)_{j,k,l} &\approx \Delta x^{-1} \left(D_z^{(2)} \phi \right)_{j,k,l} \\ &= \Delta x^{-1} \left(\phi_{j,k,l+1/2} - \phi_{j,k,l-1/2} \right), \quad |l_0 - l| = 1 \end{aligned} \quad (7c)$$

(and we use corresponding second-order difference operators for x and y derivatives, and for derivatives centered at half-integer values of j and/or k). Again, each of these difference operators acts on points confined to only one side of the fault plane, and therefore does not involve the split nodes.

[20] 4. At points located at distance $\Delta x/2$ from the fault plane, each spatial derivative is approximated by the second-order difference operator, but using split-node values corresponding to the appropriate side of the fault when values at fault-plane points are required, as in the case 2, for example,

$$\begin{aligned} (\partial_z \phi)_{j,k,l_0+1/2} &\approx \Delta x^{-1} \left(D_z^{(2)} \phi \right)_{j,k,l_0+1/2} \\ &= \Delta x^{-1} \left(\phi_{j,k,l_0+1} - \phi_{j,k,l_0}^+ \right) \end{aligned} \quad (7d)$$

$$\begin{aligned} (\partial_z \phi)_{j,k,l_0-1/2} &\approx \Delta x^{-1} \left(D_z^{(2)} \phi \right)_{j,k,l_0-1/2} \\ &= \Delta x^{-1} \left(\phi_{j,k,l_0-1}^- - \phi_{j,k,l_0-1} \right). \end{aligned} \quad (7d')$$

3.2. Fault Plane Slip Velocity and Shear Traction

[21] At points on the fault plane, we use second-order difference approximations to (5a) and (5b), and partition them into new, separate equations for the plus- and minus-side values of the split-node variables. We begin by noting that the second-order FD approximation to the x components of (5a) for an ordinary (nonsplit) node is

$$\begin{aligned} \bar{p}_{j,k,l} &\left\{ \frac{[\dot{u}_x(t + \Delta t/2)]_{j,k,l} - [\dot{u}_x(t - \Delta t/2)]_{j,k,l}}{\Delta t} \right\} \\ &= \frac{[D_x^{(2)} \sigma_{xx}(t)]_{j,k,l} + [D_y^{(2)} \sigma_{xy}(t)]_{j,k,l} + [D_z^{(2)} \sigma_{xz}(t)]_{j,k,l}}{\Delta x}, \end{aligned} \quad (8)$$

where

$$\begin{aligned} \bar{p}_{j,k,l} &= \frac{1}{4} \left(\rho_{j,k-1/2,l-1/2} + \rho_{j,k+1/2,l-1/2} \right. \\ &\quad \left. + \rho_{j,k-1/2,l+1/2} + \rho_{j,k+1/2,l+1/2} \right), \end{aligned} \quad (9)$$

with similar expressions (centered at $j + 1/2, k + 1/2, l$) for the y component of velocity. At split nodes, we write separate equations of the form (8) for each side of the fault, taking into account the shear traction vector \mathbf{T} acting at the interface, and its initial static equilibrium value \mathbf{T}^0 . To do so, we introduce the following one-sided difference approximations for $\partial_z \sigma_{xz}$, applicable to the plus and minus sides of the fault, respectively,

$$(\partial_z \sigma_{xz})_{j,k}^{\pm} \approx \pm \frac{(\sigma_{xz})_{j,k,l_0 \pm 1/2} - (T_x - T_x^0)_{j,k}}{\Delta x/2}. \quad (10)$$

Our difference equations for the split velocities \dot{u}_x^{\pm} are then

$$\begin{aligned} & \rho_{j,k}^{\pm} \left\{ \frac{[\dot{u}_x^{\pm}(t + \Delta t/2)]_{j,k} - [\dot{u}_x^{\pm}(t - \Delta t/2)]_{j,k}}{\Delta t} \right\} \\ &= \frac{[D_x^{(2)} \sigma_{xx}^{\pm}(t)]_{j,k} + [D_y^{(2)} \sigma_{xy}^{\pm}(t)]_{j,k} \pm 2 \{ [\sigma_{xz}(t)]_{j,k,l_0 \pm 1/2} - [T_x(t) - T_x^0]_{j,k} \}}{\Delta x}, \end{aligned} \quad (11)$$

where

$$\rho_{j,k}^{\pm} = \frac{1}{2} (\rho_{j,k-1/2,l_0 \pm 1/2} + \rho_{j,k+1/2,l_0 \pm 1/2}). \quad (12)$$

Finally, combining (11) with the analogous split-node partitioning of the y -component equation gives

$$\begin{aligned} [\dot{u}_y^{\pm}(t + \Delta t/2)]_{m,n} &= [\dot{u}_y^{\pm}(t - \Delta t/2)]_{m,n} + \Delta t (M_{m,n}^{\pm})^{-1} \\ &\cdot \left\{ [R_y^{\pm}(t)]_{m,n} \mp \Delta x^2 [T_y(t) - T_y^0]_{m,n} \right\}, \quad \nu = x, y, \end{aligned} \quad (13)$$

where

$$(m, n) = \begin{cases} (j, k), & \nu = x \\ (j + 1/2, k + 1/2), & \nu = y \end{cases} \quad (14)$$

$$M_{m,n}^{\pm} = \begin{cases} (\Delta x^3/4) (\rho_{j,k-1/2,l_0 \pm 1/2} + \rho_{j,k+1/2,l_0 \pm 1/2}), & \nu = x \\ (\Delta x^3/4) (\rho_{j,k+1/2,l_0 \pm 1/2} + \rho_{j+1,k+1/2,l_0 \pm 1/2}), & \nu = y \end{cases} \quad (15)$$

$$[R_{\nu}^{\pm}]_{m,n} = \Delta x^2 \left\{ \left[\frac{1}{2} D_x^{(2)} \sigma_{\nu x}^{\pm} \right]_{m,n} + \left[\frac{1}{2} D_y^{(2)} \sigma_{\nu y}^{\pm} \right]_{m,n} \pm [\sigma_{\nu z}]_{m,n,l_0 \pm 1/2} \right\}. \quad (16)$$

The slip-velocity components \dot{s}_{ν} , $\nu = x, y$, are then given by (suppressing the node indices m, n)

$$\dot{s}_{\nu}(t + \Delta t/2) = \dot{u}_{\nu}^{+}(t + \Delta t/2) - \dot{u}_{\nu}^{-}(t + \Delta t/2), \quad (17)$$

which can be integrated to obtain the slip,

$$s_{\nu}(t + \Delta t) = s_{\nu}(t) + \Delta t \dot{s}_{\nu}(t + \Delta t/2). \quad (18)$$

[22] To find the slip and slip velocity, we need to evaluate T_{ν} in (13), such that it satisfies conditions (1)–(4). Follow-

ing D05, we define \tilde{T}_{ν} as the ν component of a ‘‘trial’’ traction, i.e., the shear traction vector that would be required to enforce continuity of tangential velocity, $\dot{u}_{\nu}^{+}(t + \Delta t/2) - \dot{u}_{\nu}^{-}(t + \Delta t/2) = 0$ for ν equal to x and y , in (13). Then the resulting expression for \tilde{T}_{ν} is

$$\tilde{T}_{\nu} \equiv \frac{\Delta t^{-1} M^{+} M^{-} (\dot{u}_{\nu}^{+} - \dot{u}_{\nu}^{-}) + M^{-} R_{\nu}^{+} - M^{+} R_{\nu}^{-} + T_{\nu}^0}{\Delta x^2 (M^{+} + M^{-})} + T_{\nu}^0, \quad (19)$$

$\nu = x, y$,

where all split quantities carry nodal indices (m, n) determined by (14), and where the velocities are evaluated at $t - \Delta t/2$, and the nodal tractions and restoring forces at t .

[23] The fault jump conditions (1) and (2), evaluated at time t , are satisfied [D05] if the fault plane traction T_{ν} appearing in (13) is

$$T_{\nu} = \begin{cases} \tilde{T}_{\nu} & \nu = x, y \quad \tilde{\tau} \leq \tau_c \\ \tau_c \frac{\tilde{T}_{\nu}}{\tilde{\tau}} & \nu = x, y \quad \tilde{\tau} > \tau_c \end{cases}, \quad (20)$$

where $\tilde{\tau}$ is the magnitude of the trial traction vector defined in (19). Since the x and y components of the velocity, and therefore of the trial traction, are defined at different grid points, the evaluation of $\tilde{\tau}$ requires interpolation,

$$\begin{aligned} \tilde{\tau}_{m,n}^2 &= (\tilde{T}_{\nu})_{m,n}^2 \\ &+ \left[\frac{(\tilde{T}_{\nu})_{m+1/2,n+1/2} + (\tilde{T}_{\nu})_{m+1/2,n-1/2} + (\tilde{T}_{\nu})_{m-1/2,n+1/2} + (\tilde{T}_{\nu})_{m-1/2,n-1/2}}{4} \right]^2, \end{aligned} \quad (21)$$

where

$$\bar{\nu} = \begin{cases} y, & \nu = x \\ x, & \nu = y \end{cases}. \quad (22)$$

[24] Note that the frictional strength, τ_c , in equation (20) follows the friction law (4), which requires knowing the slip path length ℓ , obtained by time integration of \dot{s} (the magnitude of the slip velocity vector). We evaluate nodal values of \dot{s} , and then integrate to get ℓ , at every fault-plane velocity point, using the same interpolation procedure used to evaluate $\tilde{\tau}$.

3.3. Split Stress Components

[25] As noted above, and shown in Figure 1, three of the stresses components that lie on the fault plane are discontinuous (σ_{xy} , σ_{yy} and σ_{xx}), and are therefore partitioned into plus-side and minus-side stresses. Increments to the σ_{xy} stress component involve only differentiations of velocity components taken in the x and y directions, i.e., parallel to the fault plane, so the plus- and minus-side values of this stress component can be calculated from the regular (second-order) formulas, applied separately to the plus- and minus-side velocities,

$$\left(\dot{\sigma}_{xy}^{\pm} \right)_{j,k+1/2} = \mu_{j,k+1/2,l_0 \pm 1/2} \Delta x^{-1} \left(D_y^{(2)} \dot{u}_x^{\pm} + D_x^{(2)} \dot{u}_y^{\pm} \right)_{j,k+1/2} \quad (23)$$

from which we can time-integrate (6b) to obtain $\sigma_{xy}(t)$.

[26] There is an extra complication in partitioning σ_{yy} and σ_{xx} , which is that they involve a fault-normal derivative, $\partial_z \dot{u}_z$, whose ordinary second-order difference approximation involves \dot{u}_z values from both sides of the fault. To deal with this situation, we introduce plus- and minus-side fault-normal velocity values \dot{u}_z^\pm at the normal-traction (σ_{zz}) grid points on the fault (we are only considering continuous fault-normal velocity in this paper, so $\dot{u}_z^+ = \dot{u}_z^-$, but the formalism can also accommodate discontinuous normal velocity). Then we approximate $\partial_z \dot{u}_z$ with separate forward and backward differentiation formulas for the plus and minus sides, respectively,

$$(\partial_z \dot{u}_z)_{j+1/2,k}^\pm \approx \pm \frac{[(\dot{u}_z)_{j+1/2,k,l_0 \pm 1/2} - (\dot{u}_z^\pm)_{j+1/2,k}]}{\Delta x/2}. \quad (24)$$

We determine the unknown \dot{u}_z^\pm from the condition of continuous normal traction, applied to separate plus- and minus-side formulas for $\dot{\sigma}_{zz}$. The latter are obtained by combining (24) with second-order difference formulas for $\partial_y \dot{u}_y^\pm$ and $\partial_x \dot{u}_x^\pm$,

$$\begin{aligned} (\dot{\sigma}_{zz})_{j+1/2,k,l_0} = 2\Delta x^{-1} & \left(\bar{\lambda}_{j+1/2,k}^\pm + 2\bar{\mu}_{j+1/2,k}^\pm \right) \\ & \cdot \left[\pm (\dot{u}_z)_{j+1/2,k,l_0 \pm 1/2} \mp (\dot{u}_z^\pm)_{j+1/2,k} \right] \\ & + \bar{\lambda}_{j+1/2,k}^\pm \left(D_x^{(2)} \dot{u}_x^\pm + D_y^{(2)} \dot{u}_y^\pm \right)_{j+1/2,k}, \end{aligned} \quad (25)$$

where

$$\begin{aligned} \bar{\mu}_{j+1/2,k}^\pm = 4 & \left(\mu_{j,k+1/2,l \pm 1/2}^{-1} + \mu_{j+1,k+1/2,l \pm 1/2}^{-1} \right. \\ & \left. + \mu_{j,k-1/2,l \pm 1/2}^{-1} + \mu_{j+1,k-1/2,l \pm 1/2}^{-1} \right)^{-1} \end{aligned} \quad (26)$$

$$\begin{aligned} \bar{\lambda}_{j+1/2,k}^\pm = 4 & \left(\lambda_{j,k+1/2,l \pm 1/2}^{-1} + \lambda_{j+1,k+1/2,l \pm 1/2}^{-1} \right. \\ & \left. + \lambda_{j,k-1/2,l \pm 1/2}^{-1} + \lambda_{j+1,k-1/2,l \pm 1/2}^{-1} \right)^{-1}. \end{aligned} \quad (27)$$

Note that (25) represents two equations, one each for the plus and minus sides (with the same left-hand side, due to continuity of normal traction on the fault). In our case, we restrict consideration to continuous normal velocity (no fault separation), and solve (25) together with the condition $\dot{u}_z^+ = \dot{u}_z^-$. The result is

$$\begin{aligned} (\dot{u}_z^\pm)_{j+1/2,k} & = (\dot{u}_z^-)_{j+1/2,k} \\ & = \frac{A^+ (\dot{u}_z)_{j+1/2,k,l_0+1/2} + A^- (\dot{u}_z)_{j+1/2,k,l_0-1/2} - B^- + B^+}{A^+ + A^-}, \end{aligned} \quad (28)$$

where

$$\begin{aligned} A^\pm & = \frac{2}{\Delta x} \left(\bar{\lambda}_{j+1/2,k}^\pm + 2\bar{\mu}_{j+1/2,k}^\pm \right) \\ B^\pm & = \bar{\lambda}_{j+1/2,k}^\pm \frac{\left(D_x^{(2)} \dot{u}_x^\pm + D_y^{(2)} \dot{u}_y^\pm \right)_{j+1/2,k}}{\Delta x} \end{aligned} \quad (29)$$

and substitution of (28) into (25) gives σ_{zz} .

[27] Finally, with the aid of (28), we calculate $\dot{\sigma}_{xx}^\pm$ and $\dot{\sigma}_{yy}^\pm$ by formulas analogous to (25),

$$\begin{aligned} (\dot{\sigma}_{xx}^\pm)_{j+1/2,k} & = \left(\bar{\lambda}_{j+1/2,k}^\pm + 2\bar{\mu}_{j+1/2,k}^\pm \right) \Delta x^{-1} \left(D_x^{(2)} \dot{u}_x^\pm \right)_{j+1/2,k} \\ & + \bar{\lambda}_{j+1/2,k}^\pm \Delta x^{-1} \left\{ \left(D_y^{(2)} \dot{u}_y^\pm \right)_{j+1/2,k} \right. \\ & \left. + 2 \left[\pm (\dot{u}_z)_{j+1/2,k,l_0 \pm 1/2} \mp (\dot{u}_z^\pm)_{j+1/2,k} \right] \right\} \end{aligned} \quad (30)$$

$$\begin{aligned} (\dot{\sigma}_{yy}^\pm)_{j+1/2,k} & = \left(\bar{\lambda}_{j+1/2,k}^\pm + 2\bar{\mu}_{j+1/2,k}^\pm \right) \Delta x^{-1} \left(D_y^{(2)} \dot{u}_y^\pm \right)_{j+1/2,k} \\ & + \bar{\lambda}_{j+1/2,k}^\pm \Delta x^{-1} \left\{ \left(D_x^{(2)} \dot{u}_x^\pm \right)_{j+1/2,k} \right. \\ & \left. + 2 \left[\pm (\dot{u}_z)_{j+1/2,k,l_0 \pm 1/2} \mp (\dot{u}_z^\pm)_{j+1/2,k} \right] \right\}. \end{aligned} \quad (31)$$

3.4. Artificial Viscous Damping

[28] We introduce viscous damping into the equations of motion, as a device to suppresses short-wavelength oscillations arising from the numerical dispersion characteristic low-order difference approximations [Day, 1982b; Day and Ely, 2002; Day et al., 2005]. The damping is artificial, and is intended to regularize the numerical solution of the elastodynamic problem, rather than to represent a physical damping. As in D05, equations (A8) and (A18), we add terms to the elastodynamic equations that are proportional to the strain-rate components, leading to damping stresses of Kelvin-Voigt form. However, in contrast to our previous approach (in which the damping was used throughout the volume), we include this term only in the equations of motion (13) for the split nodes (a simplification introduced to minimize computer memory requirements in the current serial-code implementation). The modified expression for R^\pm with the viscous damping terms is

$$\begin{aligned} [R_\nu^\pm]_{m,n} & = \Delta x^2 \left\{ \left[\frac{1}{2} D_x^{(2)} \sigma_{\nu x}^\pm \right]_{m,n} + \left[\frac{1}{2} D_y^{(2)} \sigma_{\nu y}^\pm \right]_{m,n} \pm [\sigma_{\nu z}]_{m,n,l_0 \pm 1/2} \right\} \\ & + \Delta t \bar{\eta}_s \Delta x^2 \left\{ \left[\frac{1}{2} D_x^{(2)} \dot{\sigma}_{\nu x}^\pm \right]_{m,n} \right. \\ & \left. + \left[\frac{1}{2} D_y^{(2)} \dot{\sigma}_{\nu y}^\pm \right]_{m,n} \pm [\dot{\sigma}_{\nu z}]_{m,n,l_0 \pm 1/2} \right\}, \end{aligned} \quad (32)$$

where $\nu = x, y$, (m, n) is defined as in (14), the stress rates are evaluated at $t - \Delta t/2$, and the stresses and restoring forces at t . The damping parameter is $\bar{\eta}_s$, and the subscript s is appended to indicate that it is used at the split nodes only, and to differentiate it from the damping parameter $\bar{\eta}$ (unsubscripted) in D05 (numerical values of $\bar{\eta}_s$ and $\bar{\eta}$ are not comparable, since the latter applies throughout the volume and the former only in cells adjacent to split nodes). The introduction of the time step Δt as a factor in (32) makes the damping parameter $\bar{\eta}_s$ dimensionless. In our numerical simulations, Δt is proportional to the grid interval Δx , because Δt is constrained by the stability limit, i.e., $\Delta t \leq \text{CFL} \Delta x/\alpha$, where CFL is the Courant-Friedrich-Lewy number and α is the P wave velocity (CFL = 0.396 for the SGSN tests in this paper). The result is that the absorption-

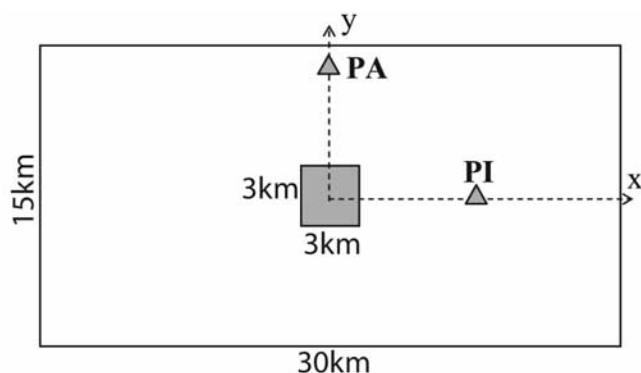


Figure 2. Fault model [from *Harris et al.*, 2004] for testing dynamic rupture simulations. The square in the center is the nucleation area. The triangles are the receivers at which we compare time-histories of slip, slip rate, and shear stress. Relative to an origin at the center of the fault, the receiver PI has y coordinate 0 and x coordinate 7.5, and the receiver PA has x coordinate 0 and y coordinate 6.0 km. The stress parameters are specified in Table 1.

wavelength spectrum for constant $\bar{\eta}_s$ scales in proportion to the grid interval (D05), ensuring that wavelengths near the grid Nyquist limit are selectively damped.

4. Numerical Test

[29] We test the SGSN approach by solving a three-dimensional (3D) problem of spontaneous rupture propagation for a planar fault embedded in a uniform infinite elastic isotropic space. The formulation and parameters of the test case correspond to Version 3 of the Southern California Earthquake Center (SCEC) benchmark problem [*Harris et al.*, 2004]. This test was selected because D05 solved this problem numerically by two difference methods, the BI method and the so-called DFM implementation of the TSN method [*Day*, 1982a, 1982b; *Day and Ely*, 2002]. They examined numerical results for a range of Δx values and found that the BI and DFM computations converged to a common solution, within well-defined tolerances which they interpreted as approximate error bounds on the solution. This permits us to use the highest-resolution DFM solution as a reference solution for assessing the accuracy of the SGSN method.

[30] The problem geometry is shown in Figure 2. We take the fault plane to be the xy plane. The shear prestress is aligned with the x axis, and the origin of the coordinate

system is located in the middle of the fault, as shown in Figure 2. The fault and prestress geometries are such that the x and y axes are axes of symmetry (or antisymmetry) for the fault slip and traction components. As a result, the xz plane undergoes purely in-plane motion, and the yz plane purely anti-plane motion.

[31] Rupture is allowed within a fault area that extends 30 km in the x direction and 15 km in the y direction. A homogeneous medium is assumed, with a P wave velocity of 6000 m/s, S wave velocity of 3464 m/s, and density of 2670 kg/m³. The distributions of the initial stresses and frictional parameters on the fault are specified in Table 1. The nucleation occurs in 3 km \times 3 km square area that is centered on the fault, as shown in Figure 2. The rupture initiates because the initial shear stress in the nucleation patch is set to be slightly (0.44%) higher than the initial static yield stress in that patch. Then the rupture propagates spontaneously through the fault area, following the linear slip-weakening fracture criterion (3)–(4).

4.1. Metrics

[32] In the work of *Dalguer and Day* [2006], the same test problem was used to assess alternative methods (Stress Glut and Thick Fault, respectively) for representing the fault. For consistency with that study, and with D05, we apply here the same three global metrics used for quantitative assessment of solution accuracy in those two papers. These are: (1) root mean square average over the fault plane of the rupture time differences between solutions, where rupture time is defined as the time at which slip velocity first exceeds 1 mm/s; (2) root mean square average, over the x and y axes, of the differences in final slip between solutions, and (3) root mean square average over the x and y axes of the differences in peak value of slip velocity. In each case, we calculate the metric of an SGSN solution with respect to the DFM solution calculated with $\Delta x = 0.05$ km (see D05), which is denoted solution DFM0.05.

4.2. Sensitivity to Damping Parameter

[33] As noted previously, artificial viscosity in the SGSN method is applied somewhat differently than in DFM, and the damping parameters in the two methods are not equivalent. Therefore we begin by examining the sensitivity of the solution to the damping parameter $\bar{\eta}_s$. We solve the test problem with different grid intervals ($\Delta x = 0.1, 0.15, 0.2, 0.25, 0.3, 0.375, 0.5$ and 0.75 km) and a range of values of $\bar{\eta}_s$, and then calculate the rupture-time metric for each case (i.e., for each $\bar{\eta}_s, \Delta x$ pair), relative to the reference solution DFM0.05.

Table 1. Dynamic Stress Parameters for Spontaneous Dynamic Rupture Simulation

Parameters	Within Fault Area of 30 km \times 15 km		
	Nucleation	Outside Nucleation	Outside Fault Area
Initial shear stress (τ_0), MPa	81.6	70.0	70.0
Initial normal stress ($-\sigma_n$), MPa	120.0	120.0	120.0
Static friction coefficient (μ_s)	0.677	0.677	infinite
Dynamic friction coefficient (μ_d)	0.525	0.525	0.525
Static yielding stress ($\tau_{cs} = -\mu_s * \sigma_n$), MPa	81.24	81.24	infinite
Dynamic yielding stress ($\tau_{cd} = -\mu_d * \sigma_n$), MPa	63.0	63.0	63.0
Dynamic stress drop ($\Delta\tau = \tau_0 - \tau_{cd}$), MPa	18.6	7.0	7.0
Strength excess (MPa) ($\tau_{cs} - \tau_0$), MPa	-0.36	11.24	infinite
Critical slip distance, m d_0	0.40	0.40	0.40

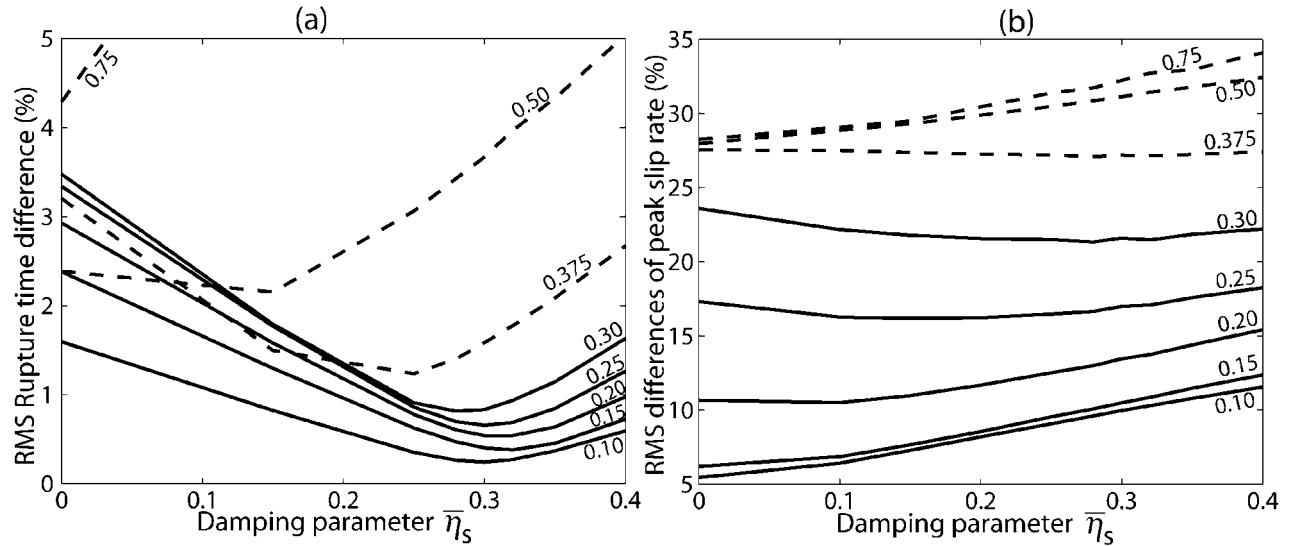


Figure 3. (a) RMS rupture time misfit as a function of the damping parameter $\bar{\eta}_s$ for each grid interval Δx . Time differences are RMS averages over the fault plane. (b) RMS peak slip rate differences as a function of the damping parameter $\bar{\eta}_s$ for each grid interval Δx . In both figures, the dashed lines correspond to lower resolution solutions ($\Delta x \geq 0.375$ km) and solid lines correspond to higher-resolution solutions $\Delta x \leq 0.3$ km.

[34] Figure 3 shows curves of RMS rupture time misfit and RMS peak slip velocity misfit, as a function of the damping parameter $\bar{\eta}_s$, for each grid interval. Dashed lines correspond to the relatively low-resolution solutions ($\Delta x \geq 0.375$ km), in which the minimum RMS rupture time misfit is larger than 1% and peak slip velocity misfit is larger than 25%, whereas solid lines correspond to solutions ($\Delta x \leq 0.3$ km) with minimum RMS rupture time misfit less than 1% and peak slip velocity less than 25%. We distinguish these two classes in Figure 3a to display the fact that the $\Delta x \leq 0.3$ km cases have settled into a systematic behavior of monotonic decrease in the rupture time misfit with decreasing Δx , for all values of $\bar{\eta}_s$ (including zero). The misfit curves for this group of higher-resolution solutions also have their minima at approximately the same damping value $\bar{\eta}_s \sim 0.3$, and have very weak dependence on $\bar{\eta}_s$ near that minimum. Moreover, both dashed- and solid-curve groups show monotonic decrease in rupture time misfit, as a function of Δx , for all $\bar{\eta}_s \geq \sim 0.2$. The sensitivity of the rupture time solutions to $\bar{\eta}_s$ diminishes with reduced grid interval: the best-resolved case in Figure 3 (with $\Delta x = 0.1$ km) has minimum misfit of $\sim 0.25\%$, and misfit remains below 0.6% through the interval $0.2 \leq \bar{\eta}_s \leq 0.4$ (and below 1.6% even for the zero-damping case). The low sensitivity to the damping parameter in the rupture time is consistent with the results obtained by D05 using the DFM method. However, as shown in Figure 3b, the peak slip velocity misfit increases with $\bar{\eta}_s$, with minimum misfit when $\bar{\eta}_s = 0$. Therefore nonzero $\bar{\eta}_s$ does not reduce the error of the peak slip velocity, as it does for the rupture time error. On the other hand, not reflected in the peak slip velocity metric is the additional beneficial effect of damping in reducing or eliminating spurious oscillations in the slip velocity time histories (time histories are discussed below).

[35] Taken together, the results in Figures 3a and 3b indicate that the SGSN method is convergent even with

$\bar{\eta}_s = 0$, but that convergence is greatly accelerated by the use of values of damping in roughly the range $0.2 \leq \bar{\eta}_s \leq 0.4$. For example, the rupture-time misfit level of 1.6% achieved in the undamped solution for $\Delta x = 0.1$ km is achieved by the damped solution (for any damping value in the interval $0.2 \leq \bar{\eta}_s \leq 0.4$) when Δx is three times as large. The results also indicate a preferred value of $\bar{\eta}_s \sim 0.3$ (and we again emphasize that the viscosity is applied differently in SGSN than in DFM, for which D05 found a preferred value of a different viscosity parameter, $\bar{\eta}$, of ~ 0.1).

4.3. Grid Dependence of Solutions

[36] We next examine SGSN solutions computed with the preferred artificial-viscosity parameter value $\bar{\eta}_s \sim 0.3$. We assess their grid-size dependence, using the three solution metrics introduced previously, for $\Delta x = 0.1$ km $\leq \Delta x \leq 0.75$ km, again calculating the metrics relative to the DFM reference solution with $\Delta x = 0.05$ km. For comparison, we also show the grid-size dependence of the DFM solutions. We name the solutions using the same convention used in D05: the calculations for $\Delta x = 0.1$ km, for example, are denoted by DFM0.1 and SGSN0.1, respectively, for the DFM and SGSN methods; and SGSN0.15 denotes the SGSN calculation with $\Delta x = 0.15$ km, with similar naming for the other cases. Grid intervals and time steps for all the solutions are shown in Table 2.

[37] The cohesive zone is the portion of the fault plane behind the crack tip where the shear stress decreases from its static value to its dynamic value and slip path-length ℓ satisfies $0 \leq \ell \leq d_0$ [e.g., *Ida*, 1972]. In the cohesive zone, shear stress and slip rate vary rapidly, and proper numerical resolution of those changes is crucial for capturing the maximum slip rates and rupture propagation speeds. To relate numerical accuracy to the degree to which the cohesive zone is resolved, we express the grid-size dependence of the solution in terms of the dimensionless ratio N_c

Table 2. Test Problem Calculations

Calculation Name	Solution Method	Grid Size Δx , km	Time Step Δt , s	Median Resolution \bar{N}_c	Rupture Time Misfit	
					RMS, %	MAX, %
SGSN0.075	SGSN	0.075	0.005	5.9	0.22	0.78
SGSN 0.1	SGSN	0.1	0.0066	4.4	0.24	1.35
SGSN0.15	SGSN	0.15	0.0099	2.9	0.40	1.56
SGSN 0.2	SGSN	0.2	0.013	2.2	0.54	1.77
SGSN0.25	SGSN	0.25	0.016	1.8	0.66	2.0
SGSN0.3	SGSN	0.3	0.02	1.5	0.83	3.13
SGSN0.375	SGSN	0.375	0.025	1.2	1.58	5.45
SGSN0.5	SGSN	0.5	0.033	0.9	3.67	10.33
SGSN0.75	SGSN	0.75	0.05	0.6	10.52	22.80
DFM0.05	DFM	0.05	0.005	8.8	0.0	0.0
DFM0.075	DFM	0.075	0.00625	5.9	0.15	0.50
DFM0.1	DFM	0.1	0.008	4.4	0.31	1.30
DFM0.15	DFM	0.15	0.0125	2.9	1.26	3.57
DFM0.2	DFM	0.2	0.016	2.2	2.72	6.41
DFM0.25	DFM	0.25	0.015	1.8	5.02	10.1
DFM0.3	DFM	0.3	0.020	1.5	8.50	15.55

introduced by D05, where N_c is the ratio of the width of the cohesive zone, Λ , to the grid interval Δx ,

$$N_c = \Lambda / \Delta x. \quad (33)$$

This ratio provides a nondimensional characterization of the resolution of a given numerical solution. As discussed at length in D05, N_c is a local measure of resolution, because Λ varies as the rupture propagates. Here we use the median value of N_c over the x axis (in-plane), denoted by \bar{N}_c , as a global measure of resolution (the choice of the x axis median is discussed in D05). The median cohesive zone size for this problem (as obtained from the reference solution DFM0.05) is 0.44 km (D05), so $\bar{N}_c = 0.44 / \Delta x$.

[38] The RMS rupture-time misfits are shown in Figure 4. Open circles correspond to the SGSN solutions, and solid circles to the DFM solutions. Note that the abscissa is denoted in two different ways on Figure 4. On the bottom, the grid size is given. On the top, we show the corresponding median cohesive-zone resolution parameter \bar{N}_c .

[39] Note in Figure 4 that the rupture-time differences for SGSN show a bilinear scaling with the grid size. The first scaling line corresponds to solutions with $\Delta x \leq 0.3$ and the second line for $\Delta x > 0.3$. The transition between these two scaling lines occurs between $\Delta x = 0.3$ and $\Delta x = 0.4$, corresponding to a grid interval slightly less than the median cohesive-zone width ($\bar{\Lambda} = 0.44$ km). In the second line, for $\Delta x \geq 0.4$, the RMS time differences exceed 1.5% and the dependence upon Δx appear to follow a power law in the grid size, with estimated exponent 2.9. As observed in Figure 4, this second line is practically parallel to the corresponding one for DFM (exponent 2.96, 90% confidence interval 2.77–3.15). The smaller multiplicative factor in the SGSN power law (for the coarser grids, $\Delta x \geq 0.4$), relative to that of DFM, may be related to the reduced numerical dispersion due to use of fourth-order spatial difference operators in SGSN (DFM uses second-order spatial differences everywhere). However, the SGSN difference operators are reduced to second order along the fault, and it is unclear how much the use of fourth-order differencing away from the fault influences rupture propagation. The

other scaling line, for $\Delta x \leq 0.3$, represents solutions with RMS time differences less than 1%. In this regime, the dependence upon Δx appears to be linear (exponent 1.1), and the misfit is comparable to the SGSN time step size. The relationship to the step size appears to be indirect, however: further numerical experiments using a small, fixed time step (i.e., Δt not proportional to Δx) give almost identical results. It appears that the power law transition for the RMS rupture-time misfit represents a precision limit proportional to the rupture transit time across one grid interval.

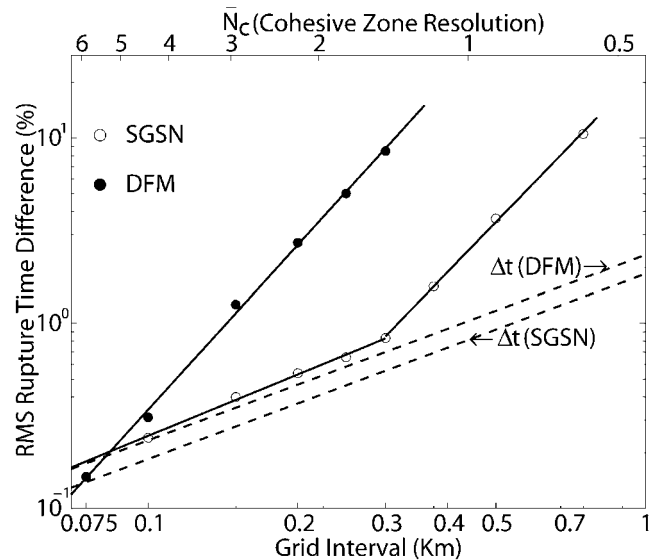


Figure 4. Differences in time of rupture, relative to reference solution, shown as a function of grid interval Δx . Differences are RMS averages over the fault plane. Open circles are SGSN solutions calculated by D05. All the solutions are relative to DFM0.05 (the smallest grid-interval DFM case). The dashed lines show the (approximate) dependence of time step Δt on Δx . The upper axis characterizes the calculations by their characteristic \bar{N}_c values, where \bar{N}_c is median cohesive zone width in the in-plane direction divided by Δx .

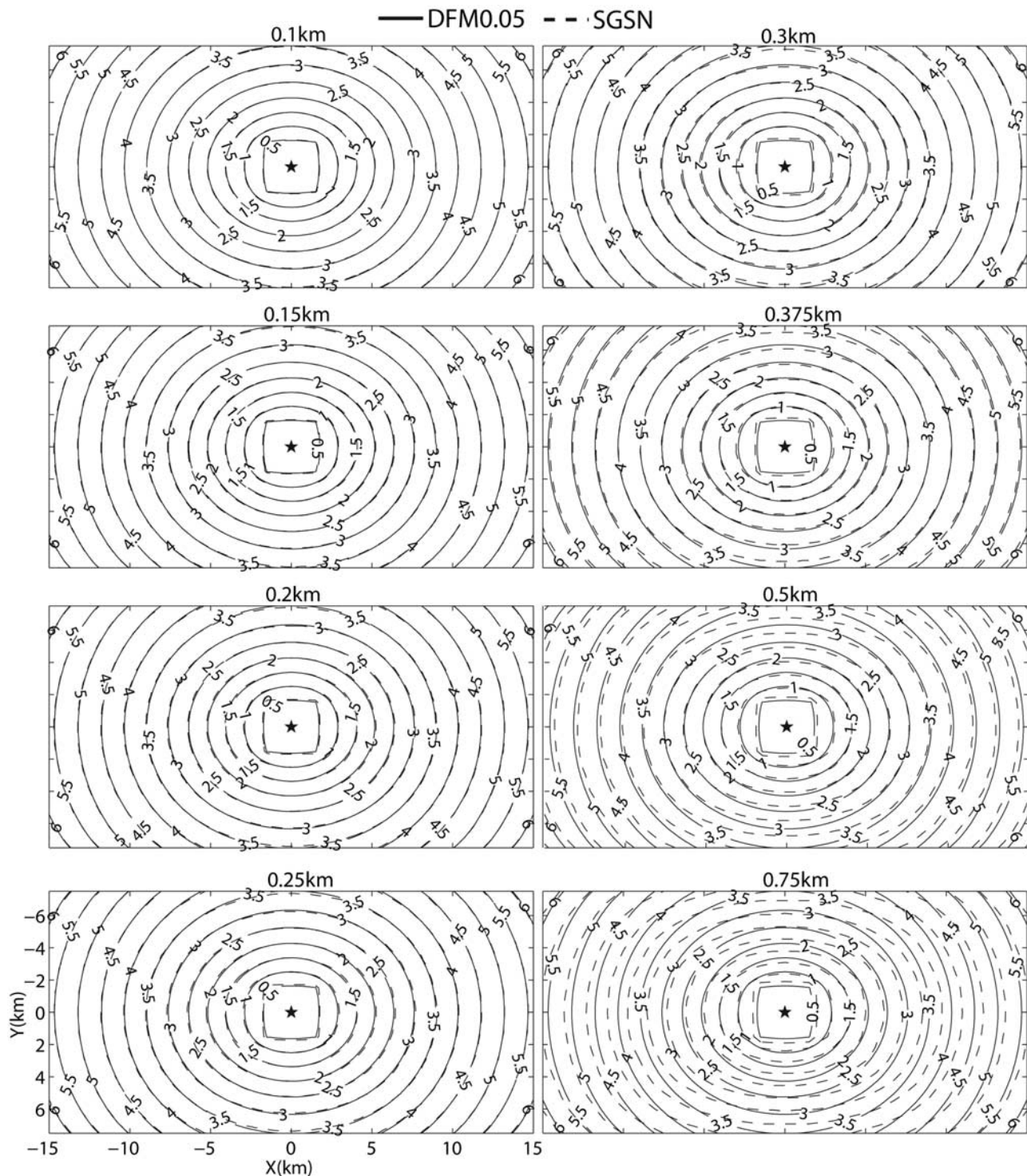


Figure 5. Contour plot of the rupture front for the spontaneous-rupture test problem, for each SGSN solution (dashed line), compared with the reference (DFM0.05) solution (solid line). The grid size of the SGSN solutions is specified on the upper side of each plot.

[40] A possible interpretation is that the SGSN method has underlying convergence rate ~ 3 ; that is, it has this convergence rate for problems with a sufficient degree of smoothness in the field variables. However, the discontinuous derivative in the slip-weakening curve used in this study is known to result in a nonsmooth stress field, and this

nonsmoothness would be expected to result in an order of accuracy lower than the nominal one that applies to smooth fields [e.g., Day et al., 2005; Kaneko et al., 2006]. The result may be timing errors of the order of the rupture transit time, truncating the Δx^3 asymptote. Accepting that view, SGSN has the same convergence rate (relative to the rupture

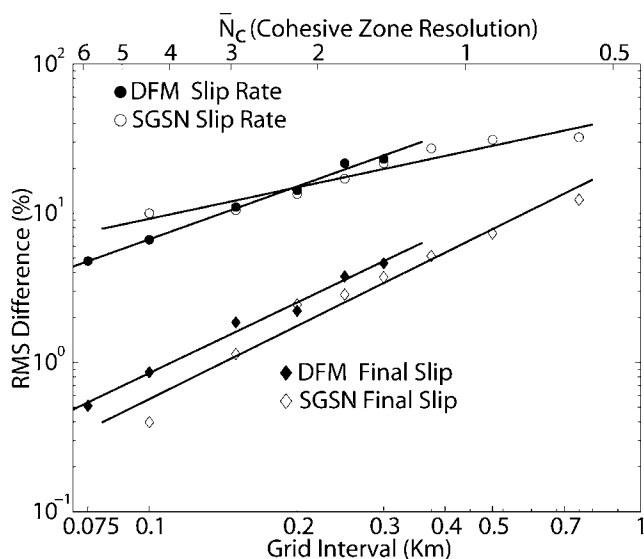


Figure 6. Differences in final slip (diamonds) and peak slip velocity (circles), relative to reference solution (DFM0.05), shown as a function of grid interval Δx . Differences are RMS averages over the x and y axes of the fault plane. Open symbols are SGSN solutions and solid symbols are DFM solutions calculated by D05.

time metric) as DFM; and, moreover, this rate is also indistinguishable from the convergence rate we determined in D05 for the BI method: all three methods share (within statistical uncertainty in the exponent estimates) the convergence rate of ~ 3 . In any event, the observation is that SGSN follows the Δx^3 asymptote until it achieves RMS rupture-time precision approximately equal to one third the rupture transit time (which happens to correspond approximately to the maximum Δt permissible for accurate computation, $\Delta t \leq \text{CFL } \Delta x/\alpha$), and it achieves that level in the test problem for $\Delta x \leq 0.3$, corresponding to $\bar{N}_c \approx 1.5$.

[41] One might suspect that the rupture-time metric gives an exaggerated misfit estimate by mainly measuring a simple time shift due to nucleation advances or delays (instead of registering primarily the more physically interesting misfits in rupture velocity). We checked this by considering the extreme case. The relative time shift between test solution and reference solution that minimizes their RMS misfit is that which makes their mean rupture times equal. We recomputed these minimized rupture-time metrics and found that the change was small in all cases, and imperceptible for the high-resolution models ($dx < 0.3$ km). Therefore simple nucleation delay does not contribute substantially to the total rupture time error. This was also shown (for a different set of test simulations) by *Dalguer and Day* [2006].

[42] The maximum difference in rupture time between DFM0.05 and SGSN0.1 is 0.0483 s, and the RMS value (averaging over the fault plane) of the difference is 0.0086 s. On the basis of the average rupture time on the fault of about 3.57 s, these maximum and RMS difference are respectively 1.35% and 0.24%. This level of precision is within our uncertainty estimate for the reference solution itself, based upon the precision of agreement achieved between the BI and DFM methods in D05. The maximum

and RMS differences between DFM0.05 and SGSN0.3 are 0.11 s (3%) and 0.029 s (0.8%), respectively (see Table 2).

[43] These quantitative results for the rupture-time metric (Figure 4) are reflected qualitatively in Figure 5, where contours of rupture time of all the SGSN solutions (dashed curves) are compared with the DFM0.05 solution (solid curves). The computed evolution of the rupture front of each SGSN solution with $\Delta x \leq 0.3$ km ($\bar{N}_c \geq \sim 1.5$) is virtually identical to that of the DFM0.05 solution. This good level of agreement is maintained at all distances and directions from the nucleation patch.

[44] Figure 6 shows the two additional measures of grid-size dependence that we evaluate: RMS misfits of final slip and maximum slip velocity, respectively, again relative to reference solution DFM0.05. Diamonds (solid for DFM, open for SGSN) denote values of the final-slip metric, circles (also solid for DFM, open for SGSN) the corresponding values for the peak slip-velocity metric. Each of these metrics appears to follow a single scaling line, albeit with more scatter than in the rupture-time case. The slip misfits for both DFM and SGSN have steeper slopes (1.57 and 1.63, respectively) than do the peak velocity misfits (1.17 and 0.7, respectively). In general, then, there is little difference between the methods for the final-slip and peak-slip-velocity metrics: both methods have roughly power-law behavior, with exponents between 1 and 2, with at most very small offsets between their asymptotes for a given metric. The RMS peak slip velocity difference falls to $\sim 9\%$ or less for $\Delta x \leq 0.1$ km ($\bar{N}_c \geq 4.4$) for DFM and SGSN. The final slip difference falls to $\sim 1\%$ or below for $\Delta x \leq 0.1$ km ($\bar{N}_c \geq 4.4$) for DFM, and for $\Delta x \leq 0.15$ km ($\bar{N}_c \geq 3$) for SGSN.

4.4. Waveform Comparison

[45] Finally, we examine the time histories of the shear stress, slip and slip rate from the test problem solutions, with DFM0.05 again as reference. These comparisons focus on two cases: (1) the highest-resolution SGSN solution, SGSN0.1, and (2) the lowest resolution SGSN case that has reached the slope 1 asymptote of the rupture-time metric, SGSN0.3 (since this case has rupture-time precision of the order of a single time step Δt). SGSN0.1 has median resolution $\bar{N}_c = 4.4$, and SGSN0.3 has median resolution a factor of 3 lower, $\bar{N}_c = 1.5$. Figure 7 shows the time histories of the stress, slip and slip rate of the SGSN0.1 and SGSN0.3 compared with the DFM0.05 at the two fault-plane points marked in Figure 2, one each on the in-plane (point PI) and anti-plane (point PA) axes, respectively. The time histories presented in Figure 7 are the direct result of our simulations, with no additional filtering applied.

[46] As seen in Figure 7, the time histories of SGSN0.1 (light solid curves) and reference solution DFM0.05 (heavy solid curves) solutions are nearly identical. The two cannot be distinguished in the plots, except in the magnified insets, where small differences can be discerned (but note the nearly perfect coincidence of the shear-stress curves for these two cases in the PI inset). Note that the slip-rate histories of SGSN0.1 are nearly free of oscillations, as are those for DFM0.05.

[47] The time histories for the lower resolution SGSN0.3 solution (dashed curves in Figure 7) differ significantly from the reference solution, despite SGSN0.3 having cap-

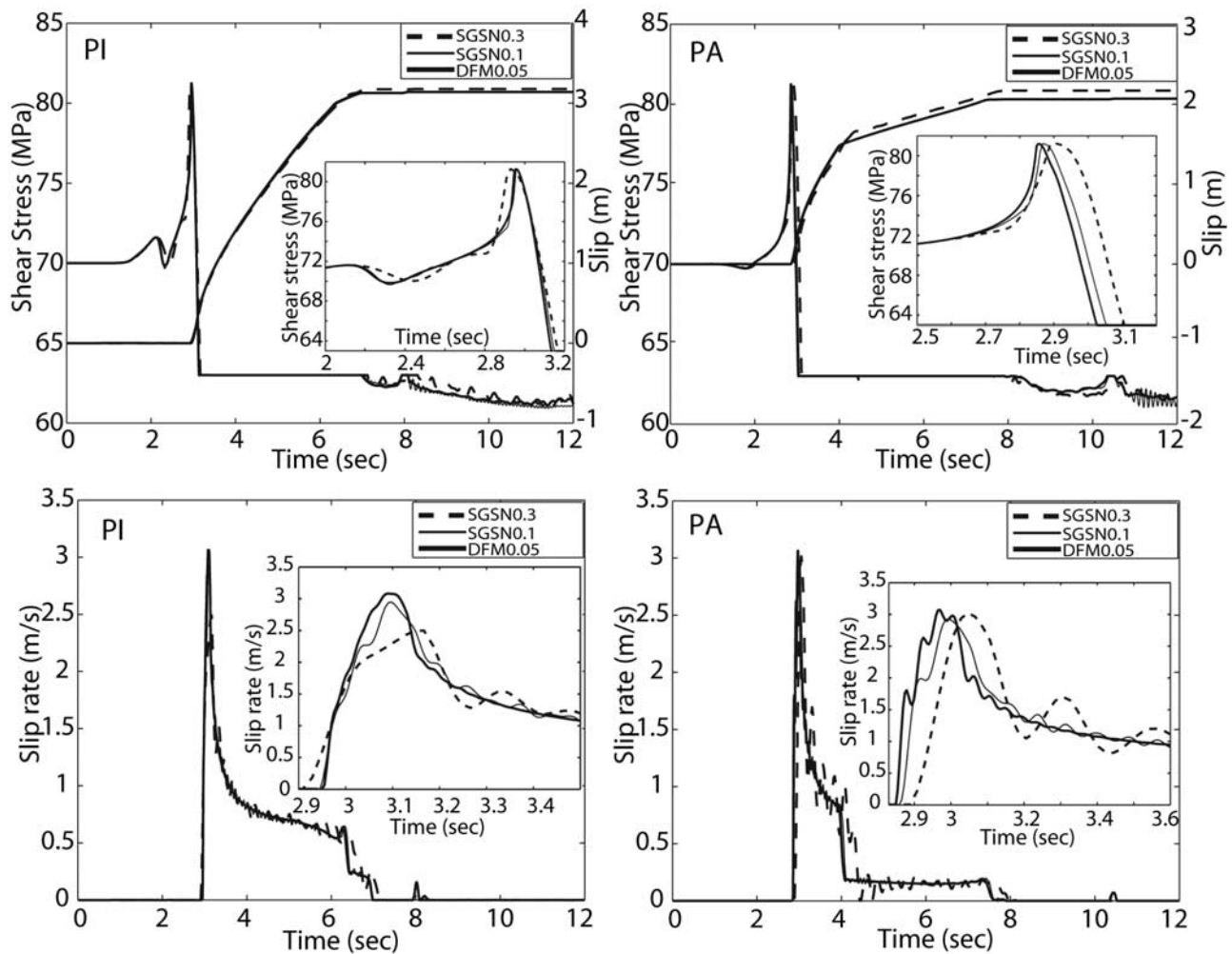


Figure 7. Time histories at the two fault plane points marked in Figure 2. PI is on the in-plane (x) axis, and PA is on the anti-plane (y) axis. Shear stress, slip, and slip velocity are shown, for solutions SGSN0.1, SGSN0.3 compared with the reference solution (DFM0.05) calculated in D05.

tured the rupture times quite accurately. SGSN0.3 shows a small discrepancy in displacement, commencing at the time that diffractions from the locked edges of the fault (“stopping phases”) are expected, most noticeably at PA, which is close to the upper edge. This discrepancy is the expected consequence of the ambiguity of order Δx in characterizing the dimensions of a discretized representation of a fault with abrupt termination, as is the case in this test problem. That is, as shown in Figure 8, the fault (in our convention) is defined as the area where rupture is allowed, so the nominal border of the fault (kept at the same location for all the solutions) has nodes in which slip occurs. The distance between this nominal border and the first fault-plane node point where no slip occurs is one grid interval Δx , inducing an order- Δx ambiguity in the stopping-phase delays. We have not pursued numerical strategies to mitigate this problem, since displacements are already highly accurate compared with the velocity pulses, and, as discussed below, it is principally the latter that appear to set the limits to solution quality. Furthermore, in problems in which rupture termination is more gradual (and perhaps more realistic), the rupture-length ambiguity is likely to be even less important.

[48] The SGSN0.3 slip velocities show notable discrepancies compared with those of the high-resolution solutions. At PA, for example, while the SGSN0.3 peak slip rate agrees well with the other two solutions, its time history has spurious oscillations, with fluctuation ampli-

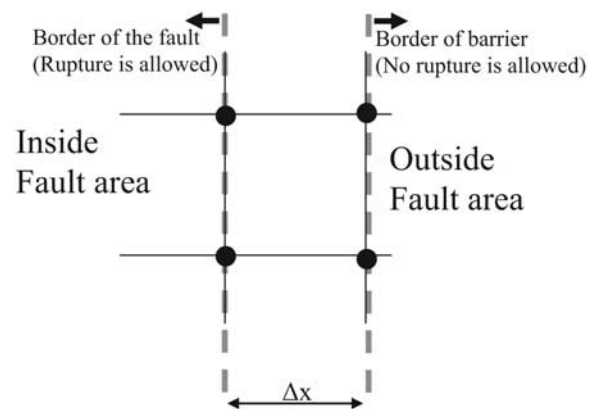


Figure 8. Schematic representation of the fault borders in the numerical simulation.

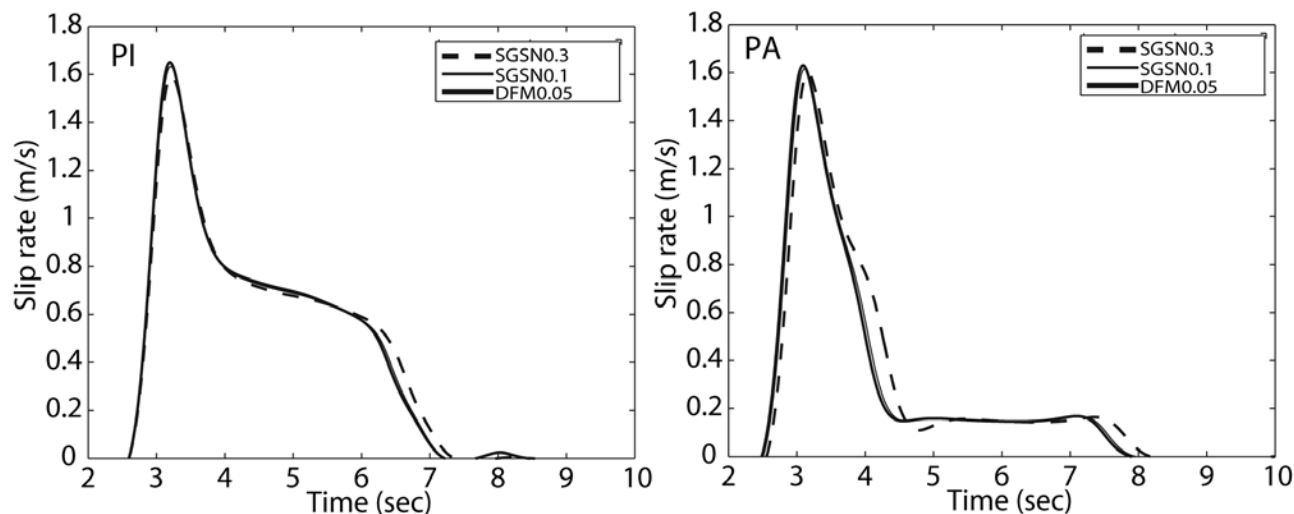


Figure 9. Slip velocity time histories for solutions SGSN0.1 and SGSN0.3, compared with the reference solution (DFM0.05) calculated in D05, at the two fault plane points marked in Figure 2. PI is on the in-plane (x) axis, and PA is on the anti-plane (y) axis. The time histories in this figure (unlike those in Figure 7) have been low-pass filtered, with corner frequency at 2 Hz.

tude of about 20% of the peak velocity. At PI, SGSN0.3 has similar, but somewhat smaller, oscillations (about 5% of peak velocity). The oscillations in the slip-velocity pulses are entirely consistent with expectations, given the very low resolution of SGSN0.3, for which the median cohesive-zone resolution is $\bar{N}_c = 1.5$; i.e., less than two grid intervals define the cohesive zone. The narrow cohesive zone permits an abrupt stress drop at the rupture front, generating stress waves of sufficiently short wavelength that they are strongly numerically dispersed by the grid. The dominant frequency of the slip-velocity oscillations of SGSN0.3 at PA, for example, corresponds to an S wavelength of less than $3\Delta x$. Even under the most optimistic assumptions (e.g., assuming that numerical dispersion is comparable to that expected for a uniformly fourth-order difference scheme), wavelengths this short are subject to severe numerical dispersion. When we low-pass filter the slip rates of the three solutions, with a 2-Hz corner frequency, corresponding to S wavelength $\sim 6\Delta x$, as shown in Figure 9, the slip-velocity time histories are nearly identical among the three solutions. The SGSN0.1 solution and DFM0.05 reference solution cannot be distinguished in Figure 9, and only significant difference between them and lower resolution SGSN0.3 is the small shift in stopping phases due to the fault-length ambiguity discussed above.

5. Discussion

[49] We have shown that the traction-at-split-node method for representing a fault plane in spontaneous rupture simulations can be effectively adapted to the staggered-grid finite difference scheme. Our staggered-grid split-node (SGSN) method partitions the discrete equations of motion in a manner very similar to that of our partly staggered split-node method, DFM [Day, 1982a, 1982b; Day and Ely, 2002; Day *et al.*, 2005], but with the addition of two new elements. First, in addition to splitting the tangential velocity compo-

nents, the method also splits the three discontinuous stress components. Second, the method interpolates the staggered “trial” traction components to form the traction vector at split nodes, as required to align the vectors of sliding friction and slip velocity. To simplify the partitioning, spatial differencing was reduced from fourth to second order along the fault plane, but in the remainder of the grid the spatial differencing scheme remains identical to conventional spatially fourth-order 3D staggered-grid schemes [e.g., Graves, 1996].

[50] With cohesive-zone resolution of $\bar{N}_c = 4.4$, SGSN is accurate relative to the reference solution DFM0.05, to within the uncertainty in the latter (as judged by the comparison of DFM with BI solutions done in D05), for both rupture-time and final-slip metrics. At this resolution of $\bar{N}_c = 4.4$, the SGSN peak slip-velocity misfit is still about a factor of 3 higher than the reference-solution uncertainty for that metric (though only about 50% higher than the DFM solution done with the same resolution value of $\bar{N}_c = 4.4$). Unfortunately, we are unable to calculate SGSN solutions with $\Delta x = 0.05$, as we were able to do with DFM, as the latter is a parallel code, and our current SGSN implementation is not.

[51] The SGSN and the DFM methods have very similar convergence properties, as indicated by the similarities of the corresponding SGSN and DFM slopes in Figures 4 and 6. These asymptotic slopes are also very similar to those obtained for BI solutions in D05. The most notable difference is the offset, by a factor of ~ 3 , between the respective Δx^3 rupture-time asymptotes for SGSN and DFM (Figure 4). That is, until its one time step threshold is approached (at about $\bar{N}_c = 1.5$), SGSN achieves a given tolerance level in RMS rupture time with \bar{N}_c about a factor of 3.0 lower than that required by DFM to achieve the same tolerance level. Remarkably, the SGSN rupture-time asymptote even has a favorable offset (a factor of ~ 1.5) relative to the BI rupture-time asymptote, given in D05. This latter result was unexpected, because the BI method only discretizes the

fault plane, incorporating the continuum response through an exact Green's function. Numerical dispersion in BI thus arises only from the time discretization, with no dispersion in the limit of very small $\Delta t/\Delta x$ (where β is the S wave speed), and dispersion is therefore likely less severe in BI than in volume discretization methods like DFM and SGSN. On the other hand, SGSN does not enjoy the same advantage (over either DFM or BI) for the final-slip and peak-slip-velocity metrics that it does for the rupture time metric. Furthermore, we made considerable effort to regularize the SGSN numerical solution by optimizing the choice of damping parameter $\bar{\eta}_s$, which probably accelerated the approach of SGSN to asymptotic behavior. Finally, the exceptionally good performance of SGSN on the rupture time metric (i.e., high accuracy with \bar{N}_c as small as ~ 1.5), would probably not carry over to friction laws with strong velocity dependence, since with $\bar{N}_c \approx 1.5$ the slip-velocity time histories still contain significant spurious oscillations. Thus, on balance, we conclude that SGSN and DFM are highly comparable in their performance.

[52] The SGSN method, like DFM, is (in its present form) limited to problems in which faults are parallel to a coordinate plane. Despite this geometrical limitation, the method may find some important applications. These would include theoretical studies demanding high accuracy and efficiency for simple fault geometries, such as theoretical studies of rupture under complex friction laws, perhaps including dynamic weakening processes such as thermal pressurization. The method also provides a straightforward means for adding spontaneous rupture capability to strong motion simulations for complex 3D geologic environments: SGSN is based upon the fourth-order staggered-grid method that has long proven to be among the most practical and efficient methods for such simulations [e.g., *Graves, 1998; Olsen et al., 1997, 2003, 2006; Pitarka et al., 1998; Wald and Graves, 1998*]. The SGSN method provides an efficient and accurate means of adding spontaneous rupture capability to those schemes while retaining their other computational advantages.

[53] Apart from demonstrating the method's potential utility, the SGSN results have an additional implication. *Dalguer and Day [2006]* tested two methods that have previously been proposed for adding spontaneous rupture capability to staggered-grid finite difference codes. Both of these previous methods approximate the fault as a finite-thickness inelastic zone. Dalguer and Day found that both methods had relatively poor convergence properties compared with the split-node DFM method. One of the inelastic-zone methods could not even achieve qualitatively meaningful solutions to the 3D test problem with any grids intervals that were computationally feasible. The second inelastic-zone method achieved test-problem solutions that were qualitatively meaningful, and quantitatively reliable to within a few percent, but the grid-interval requirements for accuracy rendered the method computationally inefficient relative to the DFM split-node approach with which it was compared. This raised the question of whether the poor performance reflected principally the limitations of the inelastic-zone fault representation schemes, or reflected an inherent unsuitability of the staggered-grid geometry to the spontaneous rupture problem. The results in this paper provide an answer to this

question: The similarity of results between SGSN and DFM (which also uses the split-node fault representation, but has the quite different partly staggered-grid geometry) demonstrates that accuracy in finite difference solutions to the spontaneous rupture problem is controlled principally by the scheme used to represent the fault discontinuity, and is relatively insensitive to the grid geometry used to represent the continuum.

[54] Finally, there are possible generalizations of the SGSN method that might become practical in the future. For example, the use of a staggered grid in elastodynamics calculations is not fundamentally limited to Cartesian grid geometries, and the SGSN approach would be equally applicable to a non-Cartesian staggered-grid code, should one be developed. Such a method would accommodate nonplanar faults. Nor is there anything fundamental about our decision to reduce the difference operators to second order at the fault. An alternative would be to use separate, one-sided fourth-order differences on each side of the fault. Like the current method, such a scheme would also partition naturally into separate difference equations for the two sides of each split node.

6. Conclusions

[55] The traction-at-split-node method for spontaneous rupture simulations has been successfully adapted to the velocity-stress staggered-grid finite difference scheme. Previous implementations of split nodes had been restricted to unstaggered or partly staggered grids, where node splitting was used only to introduce discontinuous velocities. In contrast, the staggered-grid implementation introduces both velocity and stress discontinuities via split nodes. The resulting method, SGSN, appears to be convergent, with convergence rates relative to rupture-time, final-slip, and peak-slip-velocity metrics that are very similar to the corresponding rates we have found (see D05) for both the partly staggered split-node method DFM and the boundary integral method. The SGSN method gives very accurate solutions (in the sense that errors are comparable to the uncertainties in the reference solution) when the median resolution of the cohesive zone is 4.4 grid points ($\bar{N}_c \approx 4.4$). Combined with results for other grid types (D05) and other fault-discontinuity approximations [*Dalguer and Day, 2006*], the SGSN results demonstrate that accuracy in finite difference solutions to the spontaneous rupture problem is controlled principally by the scheme used to represent the fault discontinuity, and is relatively insensitive to the grid geometry used to represent the continuum. The method provides an efficient and accurate means of adding spontaneous rupture capability to velocity-stress staggered-grid finite difference codes, while retaining the computational advantages of those codes for problems of wave propagation in complex media.

[56] **Acknowledgments.** We thank Joe Andrews, Raul Madariaga, and Jean Paul Ampuero, as well as Associate Editor Eric Dunham, for constructive comments and very helpful reviews that improved the presentation of the paper. We are also very grateful to Arben Pitarka for providing us with his staggered-grid FD code. This work was supported by the National Science Foundation, under grants ATM-0325033 and EAR-0122464, and by the Southern California Earthquake Center (SCEC). SCEC is funded by NSF Cooperative Agreement EAR-0106924 and USGS Cooperative Agreement 02HQAG0008. SCEC contribution 988.

References

- Andrews, D. J. (1973), A numerical study of tectonic stress release by underground explosions, *Bull. Seismol. Soc. Am.*, *63*, 1375–1391.
- Andrews, D. J. (1976a), Rupture propagation with finite stress in antiplane strain, *J. Geophys. Res.*, *81*, 3575–3582.
- Andrews, D. J. (1976b), Rupture velocity of plane-strain shear cracks, *J. Geophys. Res.*, *81*, 5679–5687.
- Andrews, D. J. (1999), Test of two methods for faulting in finite-difference calculations, *Bull. Seismol. Soc. Am.*, *89*, 931–937.
- Dalguer, L. A., and S. M. Day (2004), Split nodes and fault zone models for dynamic rupture simulation, *Eos Trans. AGU*, *85*(47), Fall Meet. Suppl., Abstract S41A-0944.
- Dalguer, L. A., and S. M. Day (2006), Comparison of fault representation methods in finite difference simulations of dynamic rupture, *Bull. Seismol. Soc. Am.*, *96*, 1764–1778.
- Dalguer, L. A., K. Irikura, J. Riera, and H. C. Chiu (2001), The importance of the dynamic source effects on strong ground motion during the 1999 Chi-Chi (Taiwan) earthquake: Brief interpretation of the damage distribution on buildings, *Bull. Seismol. Soc. Am.*, *95*, 1112–1127.
- Dalguer, L. A., K. Irikura, and J. D. Riera (2003a), Simulation of tensile crack generation by three-dimensional dynamic shear rupture propagation during an earthquake, *J. Geophys. Res.*, *108*(B3), 2144, doi:10.1029/2001JB001738.
- Dalguer, L. A., K. Irikura, and J. D. Riera (2003b), Generation of new cracks accompanied by the dynamic shear rupture propagation of the 2000 Tottori (Japan) earthquake, *Bull. Seismol. Soc. Am.*, *93*, 2236–2252.
- Das, S., and K. Aki (1977), Fault planes with barriers: A versatile earthquake model, *J. Geophys. Res.*, *82*, 5648–5670.
- Day, S. M. (1977), Finite element analysis of seismic scattering problems, Ph.D. dissertation, Univ. of Calif., San Diego.
- Day, S. M. (1982a), Three-dimensional finite difference simulation of fault dynamics: Rectangular faults with fixed rupture velocity, *Bull. Seismol. Soc. Am.*, *72*, 705–727.
- Day, S. M. (1982b), Three-dimensional simulation of spontaneous rupture: The effect of nonuniform prestress, *Bull. Seismol. Soc. Am.*, *72*, 1881–1902.
- Day, S. M., and G. P. Ely (2002), Effect of a shallow weak zone on fault rupture: Numerical simulation of scale-model experiments, *Bull. Seismol. Soc. Am.*, *92*, 3006–3021.
- Day, S. M., L. A. Dalguer, N. Lapusta, and Y. Liu (2005), Comparison of finite difference and boundary integral solutions to three-dimensional spontaneous rupture, *J. Geophys. Res.*, *110*, B12307, doi:10.1029/2005JB003813.
- Fukuyama, E., and R. Madariaga (1998), Rupture dynamic of a planar fault in a 3D elastic medium: Rate- and slip-weakening friction, *Bull. Seismol. Soc. Am.*, *88*, 1–17.
- Graves, R. W. (1996), Simulating seismic wave propagation in 3D elastic media using staggered-grid finite differences, *Bull. Seismol. Soc. Am.*, *86*, 1091–1106.
- Graves, R. W. (1998), Three-dimensional finite-difference modeling of the San Andreas fault: Source parameterization and ground motion levels, *Bull. Seismol. Soc. Am.*, *88*, 881–897.
- Harris, R. A., and S. M. Day (1999), Dynamic three-dimensional simulations of earthquakes on en echelon faults, *Geophys. Res. Lett.*, *26*, 2089–2092.
- Harris, R. A., et al. (2004), The source physics of large earthquakes: Validating spontaneous rupture methods, *Eos Trans. AGU*, *85*(47), Fall Meet. Suppl., Abstract S12A-05.
- Ida, Y. (1972), Cohesive force across the tip of a longitudinal-shear crack and Griffith's specific surface energy, *J. Geophys. Res.*, *77*, 3796–3805.
- Kaneko, Y., N. Lapusta, and J. P. Ampuero (2006), Spectral element modeling of earthquake nucleation and spontaneous rupture on rate and state faults paper presented at 2006 SCEC Annual Meeting, Southern Calif. Earthquake Cent., Los Angeles.
- Kostrov, B. V. (1964), Self-similar problem of propagation of shear crack, *J. Appl. Math. Mech.*, *28*, 1077–1087.
- Kostrov, B. V. (1966), Unsteady propagation of longitudinal shear cracks, *J. Appl. Math. Mech.*, *30*, 1241–1248.
- Levander, A. R. (1988), Fourth-order finite-difference P-SV seismograms, *Geophysics*, *53*, 1425–1436.
- Madariaga, R. (1976), Dynamics of an expanding circular fault, *Bull. Seismol. Soc. Am.*, *66*, 639–666.
- Madariaga, R., K. Olsen, and R. Archuleta (1998), Modeling dynamic rupture in a 3D earthquake fault model, *Bull. Seismol. Soc. Am.*, *88*, 1182–1197.
- Moczo, P., J. Kristek, V. Vavryčuk, R. J. Archuleta, and L. Halada (2002), 3D heterogeneous staggered-grid finite-difference modeling of seismic motion with volume harmonic and arithmetic averaging of elastic moduli and densities, *Bull. Seismol. Soc. Am.*, *92*, 3042–3066.
- Moczo, P., J. O. A. Robertsson, and L. Eisner (2006), The finite-difference time-domain method for modeling of seismic wave propagation, in *Advances in Wave Propagation in Heterogeneous Earth*, *Adv. Geophys. Ser.*, edited by R.-S. Wu and V. Maupin, chap. 8, Elsevier, New York.
- Olsen, K. B., R. Madariaga, and R. Archuleta (1997), Three dimensional dynamic simulation of the 1992 Landers earthquake, *Science*, *278*, 834–838.
- Olsen, K. B., S. M. Day, and C. R. Bradley (2003), Estimation of Q for long-period (>2 s) waves in the Los Angeles Basin, *Bull. Seismol. Soc. Am.*, *93*, 627–638.
- Olsen, K. B., S. M. Day, J. B. Minster, Y. Cui, A. Chourasia, M. Faerman, R. Moore, P. Maechling, and T. Jordan (2006), Strong shaking in Los Angeles expected from southern San Andreas earthquake, *Geophys. Res. Lett.*, *33*, L07305, doi:10.1029/2005GL025472.
- Pitarka, A. (1999), 3D elastic finite-difference modeling of seismic motion using staggered grid with nonuniform spacing, *Bull. Seismol. Soc. Am.*, *89*, 54–68.
- Pitarka, A., K. Irikura, T. Iwata, and H. Sekiguchi (1998), Three-dimensional simulation of the near-fault ground motion for the 1995 Hyogo-ken Nanbu (kobe), Japan, earthquake, *Bull. Seismol. Soc. Am.*, *88*, 428–440.
- Wald, D. J., and R. W. Graves (1998), The seismic response of the Los Angeles basin, California, *Bull. Seismol. Soc. Am.*, *88*, 337–356.

L. A. Dalguer and S. M. Day, Department of Geological Sciences, San Diego State University, 5500 Campanile Dr., San Diego, CA 92182, USA. (ldalguer@moho.sdsu.edu)